Elsevier Editorial System(tm) for Medical Engineering & Physics

Manuscript Draft

Manuscript Number:

Title: Model-Based Tracking of the Bones of the Foot: A Biplane Fluoroscopy Validation Study

Article Type: Paper

Section/Category: Regular Issue Paper

Keywords: biplane fluoroscopy; model-based; bone-based; validation; foot and ankle

Corresponding Author: Dr. William R Ledoux, PhD

Corresponding Author's Institution: VA Puget Sound

First Author: Joseph M Iaquinto, PhD

Order of Authors: Joseph M Iaquinto, PhD; Matthew W Kindig, MS; David R Haynor, MD, MPH; QuocBau Vu, BS; Nathan Pepin, BS; Richard Tsai, MS; Bruce J Sangeorzan, MD; William R Ledoux, PhD

Abstract: Measuring foot kinematics using optical motion capture is technically challenging due to skin tissue artifact and small bone size. We present a validation of our biplane X-ray system, demonstrating its capacity to track foot bones. Using precision stages we imaged two sets of tali, calcanei and first metatarsals, with imbedded beads, through 30 unique positions. Bone- and bead-based algorithms were employed for semi-automatic tracking. Translational and rotational positions were compared to precision stages to determine performance. For each bone, 300 frames were analyzed. Model-based: The resulting overall translational bias of the six bones was 0.058 mm with a precision of ± 0.049 mm. The overall rotational bias of the six bones was 0.291° with a precision of ± 0.268°. Bead-based: the overall translational bias was 0.037 mm with a precision of ± 0.032 mm and for rotation was 0.292° with a precision of ± 0.263°. We have validated the potential of our system to track foot bone motion. Bead-and bone-based tracking have comparable errors vs. the precision stages. This X-ray based methodology can significantly benefit the field of image-based measurement and diagnostics by allowing the direct measure of foot bone kinematics during activities such as gait.

VA REHABILITATION RESEARCH AND DEVELOPMENT CENTER OF EXCELLENCE FOR LIMB LOSS PREVENTION AND PROSTHETIC ENGINEERING

VA Puget Sound Health Care System
1660 S. Columbian Way MS 151
Seattle, WA 98108
Phone: (206) 768-5347
Fax: (206) 764-2127

To: Dr. Richard A. Black
University of Strathclyde, Glasgow, UK
From: William R. Ledoux, PhD
Date: 11/18/15
Re: Article submission

Dear Dr. Black:

I would like to submit an article titled "Model-Based Tracking of the Bones of the Foot: A Biplane Fluoroscopy Validation Study" to Medical Engineering & Physics as a Paper. My co-authors were fully involved in the study and preparation of the manuscript. The material within has not been and will not be submitted for publication elsewhere.

Please let me know if you require anything further.

Best regards,

William Ledoux

***Declaration form**

Journal: MEDICAL ENGINEERING & PHYSICS

Title of Paper: Model-Based Tracking of the Bones of the Foot: A Biplane Fluoroscopy Validation Study

Declarations

The following additional information is required for submission. Please note that this form runs over two pages and failure to respond to these questions/statements will mean your submission will be returned to you. **If you have nothing to declare in any of these categories then this should be stated.**

Conflict of interest
All authors must disclose any financial and personal relationships with other people or organisations that could inappropriately influence (bias) their work. Examples of potential conflicts of interest include employment, consultancies, stock ownership, honoraria, paid expert testimony, patent applications/registrations, and grants or other funding.

Conflicts of Interest

No conflicts of interest.

Please state any sources of funding for your research

Department of Veterans Affairs Rehabilitation Research and Development Service

Ethical Approval

Work on human beings that is submitted to *Medical Engineering & Physics* should comply with the principles laid down in the Declaration of Helsinki; Recommendations guiding physicians in biomedical research involving human subjects. Adopted by the 18th World Medical Assembly, Helsinki, Finland, June 1964, amended by the 29th World Medical Assembly, Tokyo, Japan, October 1975, the 35th World Medical Assembly, Venice, Italy, October 1983, and the 41st World Medical Assembly, Hong Kong, September 1989. You should include information as to whether the work has been approved by the appropriate ethical committees related to the institution(s) in which it was performed and that subjects gave informed consent to the work.

DOES YOUR STUDY INVOLVE HUMAN SUBJECTS? Please cross out whichever is not applicable.

No

If your study involves human subjects you MUST have obtained ethical approval.
Please state whether Ethical Approval was given, by whom and the relevant Judgement's reference number

DOES YOUR STUDY INVOLVE ANIMAL SUBJECTS? Please cross out whichever is not applicable.

No

If your study involves animals you must declare that the work was carried out in accordance with your institution guidelines and, as appropriate, in accordance with the EU Directive 2010/63/EU**.** http://eur-lex.europa.eu/legal-content/EN/TXT/?uri=CELEX:32010L0063

This information must also be inserted into your manuscript under the acknowledgements section prior to the References.

If you have no declaration to make please insert the following statements into your manuscript:

Competing interests: None declared

Funding: None

Ethical approval: Not required

***Referee Suggestions**

1. Professor Chris Nester
Associate Head Research & Innovation
Research Lead: Foot & Ankle Biomechanics
School of Health Sciences
Office PO 32: Brian Blatchford Building
University of Salford
M6 6PU, UK
t: (++ 44) 0161 295 2275
m:07780 568054
e: c.j.nester@salford.ac.uk

2. Dr. Toni Arndt
Dept. Orthopedic Surgery K54
Huddinge University Hospital
141 86 Huddinge
Sweden
Tel: x46-8-585 87154
Fax: x46-8-711 4292
toni.arndt@karo.ki.se

3. Dr.ir. Bart L. Kaptein
Leids Universitair Medisch Centrum Gebouw 1, Kamer J11-R-73
Postzone J11-R Postbus 9600 2300 RC Leiden
Bezoekadres: Albinusdreef 2 2333 ZA Leiden
Tel: +31(0)71 526 4542
B.L.Kaptein@lumc.nl

4. Stephen Urry
drsteveurry@yahoo.co.uk

5. Thomas Jenkyn
Department of Mechanical & Materials Engineering
Spencer Engineering Building,
Room SEB 2075
Western University
Tel: 519-661-2111 ext. 88339
tjenkyn@uwo.ca

***Highlights (for review)**

- A model-based bone tracking algorithm was validated for foot and ankle bones.
- The translational accuracy of the system was 0.058 mm with a precision of ± 0.049 mm.
- The rotational accuracy of the system was 0.291° with a precision of ± 0.268°.
- Bead-tracking errors were comparable compared to the precision stage.

Model-Based Tracking of the Bones of the Foot: A Biplane Fluoroscopy Validation Study

Joseph M. Iaquinto[1, 2], Matthew W. Kindig[1], David R. Haynor[3], QuocBao Vu[2], Nathan Pepin[2], Richard Tsai[1], Bruce J. Sangeorzan[1,4], and William R. Ledoux[1,2,4]

[1]RR&D Center of Excellence for Limb Loss Prevention and Prosthetic Engineering, Department of Veterans Affairs, Seattle, WA 98108, USA

Departments of [2]Mechanical Engineering, [3]Radiology, and [4]Orthopaedics & Sports Medicine, University of Washington, Seattle, WA 98195, USA

Address correspondence to:

William R. Ledoux, PhD

VA Puget Sound, ms 151

1660 S. Columbian Way

Seattle, WA 98108

206-768-5347(v), 206-764-2127(f), wrledoux@uw.edu

Keywords: biplane fluoroscopy; model-based; bone-based; validation; foot and ankle

Abstract

Measuring foot kinematics using optical motion capture is technically challenging due to skin tissue artifact and small bone size. We present a validation of our biplane X-ray system, demonstrating its capacity to track foot bones. Using precision stages we imaged two sets of tali, calcanei and first metatarsals, with imbedded beads, through 30 unique positions. Bone- and bead-based algorithms were employed for semi-automatic tracking. Translational and rotational positions were compared to precision stages to determine performance. For each bone, 300 frames were analyzed. Model-based: The resulting overall translational bias of the six bones was 0.058 mm with a precision of ± 0.049 mm. The overall rotational bias of the six bones was 0.291° with a precision of ± 0.268°. Bead-based: the overall translational bias was 0.037 mm with a precision of ± 0.032 mm and for rotation was 0.292° with a precision of ± 0.263°. We have validated the potential of our system to track foot bone motion. Bead-and bone-based tracking have comparable errors vs. the precision stages. This X-ray based methodology can significantly benefit the field of image-based measurement and diagnostics by allowing the direct measure of foot bone kinematics during activities such as gait.

Abbreviations

CPU: central processing unit

CMM: coordinate measurement machine

DLT: direct linear transformation

DDR: digitally reconstructed radiograph

GPU: graphic processing unit

GUI: graphically user interface

NCC: normalized correlation coefficient

RMSE: root mean square error

STA: skin tissue artifact

Introduction

The joints within the lower extremity: the hip, knee and – the focus of this work – the foot and ankle complex, play a primary role in locomotion and mobility but their function can be challenging to study. The common standard in the field of joint kinematics is optical motion capture. These systems utilize reflective surface markers and a measurement volume flooded with infrared light in order to track the motion of body segments. Optical motion capture has been used to study the lower extremity through the development of numerous marker models [1-5]. These models have been used to quantify gait kinematics in normal subjects [6, 7], in patients with ankle arthrosis [8], and in patients with adult-acquired flatfoot deformity [9].

However, an overall limitation of optical motion capture is skin tissue artifact (STA) – the error associated with the non-rigid motion between the skin-mounted location of an optical marker and the underlying bony landmark it is nominally tracking [10-16]. Cappello et al. demonstrated that (at the knee) a single calibration of landmark locations yields a root-mean-square error (RMSE) which averaged 3.7° to 6.4° in rotation and 6.3 mm to 12.9 mm in translation. Their attempts to compensate by considering two kinematic calibration endpoints and linearly interpolating between them reduced the average RMSE to 1.4° to 1.6° in rotation and 2.0 mm to 2.8 mm in translation [10]. Tranberg and Karlsson measured STA using metal markers and a fluoroscopy system. They found that marker movement was dependent on marker location – with distal forefoot markers demonstrating less motion (a maximum 1.8 mm) than proximal hind and midfoot markers (a maximum of 4.3 mm) [11]. The phase of the gait cycle was also found to affect STA. Shultz, Kedgley, and Jenkyn found greater marker STA error in triad origin translation in toe-off, than in heel-strike or mid-stance for the calcaneus and navicular (e.g., 12.1 ± 0.3 mm at toe-off vs. 5.9 ± 7.3 mm at heel-strike for the calcaneus) [12]. These location and movement-specific variabilities in overall optical motion capture error are worth consideration by themselves, but there are additional challenges present when studying the foot and ankle. A study by Nester *et al*. used bone pins to compare to two optical marker techniques (individually mounted skin markers and rigid marker plates mounted to skin). Their study found errors that were specific to the particular joint and plane of motion. Comparing any two of their three protocols (individual, plate and bone motion) during stance, the results showed an average maximum difference in error that was >3% in 100% of the data, >5% in 73% of the data and >8% in 23% of the data [15].

Two additional specific limitations of optical motion capture arise when considering the anatomy of the foot and ankle. The first is that an important bone in the ankle (the talus) possesses no near-surface landmarks due to its depth; this renders it unsuitable for optical motion capture and thus prevents the separation of ankle and subtalar joint motions. The second specific limitation is that many of the bones of the foot are very small, and are therefore

technically challenging to affix adequate markers to without experiencing significant marker visual overlap and merging; this requires the grouping of several bones into multi-bone kinematic segments, necessitating a simplification of the kinematics within the foot and ankle from bones to regions, a paradigm ill-suited for joint-specific study. In summary, optical motion capture is limited primarily due to STA, which is influenced by marker location and gait phase; there are also secondary concerns due to bone depth and size. Present through all of the mentioned studies are errors that may be particularly problematic when considering the magnitude of joint motions that are associated with clinical significance.

Biplane fluoroscopy (also known as dynamic stereo X-ray [16], dual-orthogonal fluoroscopy [17], etc.) is a rapidly growing technique which can visualize and track the motion of bones directly. By directly imaging the bones, some of the deficiencies of optical motion capture – including difficulties in marker tracking due to STA – are overcome. Direct visualization with fluoroscopy also resolves challenges with tracking deep bones and small bones.

Biplane fluoroscopy has been used elsewhere to study the hip [18, 19], the knee [17, 20, 21] and the ankle [22-24]. Due to the relative novelty of this technology, the lack of standardized commercial availability of processing software, and the strong influence that the anatomy of interest has on the potential bias of such systems – the need to validate biplane fluoroscopy techniques is strongly acknowledged in the community. Numerous laboratories have published literature describing their validation methods in order to support the findings and impact of their subsequent research [19, 21, 24-30]. Most studies use bead-based (also called marker-based) tracking as a reference for their bone-based (also called model-based) results, where the position of the beads is the "gold standard" by which their bone tracking is compared to. At the hip, Lin et al. reported an bias ± precision of 0.60 ± 0.75 mm and 0.69 ± 0.85° for the hip in static poses [19]. Anderst et al. tracked the femur and tibia with bias ranging (in their static trials), overall, from -0.37 mm to 0.14 mm and precision ranging from 0.03 mm to 0.08 mm when comparing their bead-based tracking results to model-based [21]. Using a similar method, Bey et al. reported values at the knee for the patella and femur with a bias which ranged overall from -0.174 mm to 0.248 mm, and a precision ranging from 0.023 mm to 0.062 mm for static trials [25]. In the ankle, Caputo et al. determined an average error in displacement of 0.04 ± 0.11 mm, with an average error in rotation of 0.2 ± 0.1° [23]. Also in the ankle, Wang et al. reported a mean translational bias of 0.03 mm ± 0.35 mm and a mean rotational bias of 0.25° ± 0.81° across all trials and for all bones (tibia, talus and calcaneus) [24].

Our laboratory has developed a biplane fluoroscopy system to study foot and ankle kinematics. We have previously reported the results of our hardware tuned to optimize marker-based tracking using a precision translation / rotation stage [31]. The objective of this work was to develop and validate a model-based tracking technique applied to the foot. A secondary

objective was to evaluate marker based tracking performance. Both objectives utilize a precision stage as a "gold standard". With the use of a numerical optimization algorithm, we hypothesized that we could track the position and rotation of bones of the foot (talus, calcaneus and first metatarsal) with sub-millimeter and sub-degree bias and precision.

Methods

System Overview

Biplane fluoroscopy works by using, in brief: (a) a pair of 2-dimensional (2D) images of subject's bones during functional tasks taken from different perspectives; (b) a separate imaging session (commonly CT or MRI) collects high resolution bone geometry to build 3-dimensional (3D) digital bone models; (c) digital volumetric bone models are used to mathematically generate an artificial X-ray image in a virtual environment; (d) the pose of the digital bone models are adjusted until the artificial X-ray image "matches" the 2D images taken during subject trials. This methodology yields a 3D bone position for each frame, which can then be used to calculate joint kinematics over a dynamic exercise such as gait. More detail is included in the bone position optimization section below.

Our biplane system hardware consists of two modified Philips BV Pulsera C-arm fluoroscopes (Philips Medical Systems, Best, the Netherlands), arbitrarily named the "blue" and "green" systems. The fluoroscopes' digital cameras were replaced with high speed digital videocameras (Phantom v5.2, Vision Research, Wayne NJ) capable of a 1000 Hz framerate at an 1152 x 896 pixel resolution. The fluoroscopes and digital cameras are connected to a laboratory PC which coordinates the activation of the fluoroscope systems and the collection of data through custom lab interface hardware. The performance of the hardware has been previously described [31].

Session Setup

Prior to a session of testing, two sets of data are captured that are necessary for pre-processing of the experimental data. The first data set are images of a *distortion correction plate* which is affixed to the image intensifiers. This rigid aluminum plate has a precision machined grid of 3 mm holes spaced 15 mm apart. Additionally there is a unique pattern of 5 mm holes present to define the plate orientation (Figure 1). The second data set are images of a *localizer / calibration block*. This rigid plastic block is made of a stable radiolucent polymer (R1/HG3000, GoldenWest Mfg., Inc.; Cedar Ridge, CA). The localizer block has 15 tantalum beads of varying diameters permanently seated within it at known locations to form a unique 3D pattern (Figure 2). True bead centroids and diameters were determined to within 0.007 mm using a coordinate

measuring machine (CMM, Global Performance Model, Hexagon Metrology; North Kingstown, RI). More details are provided in the pre-processing section, and in the prior publication [31].

Validation Trials

Two calcanei, tali, and first metatarsals were harvested from cadaveric donors (three females aged: 72, 80 and 82 years old weighing 53, 73 and 63 kg, respectively). The bones were imbedded in foam blocks (Figure 3, top). These blocks are rigid to prevent movement of the imbedded bones, and are of low radiodensity to prevent image artifact; additionally a plastic "wand" affixed to the block served as an attachment point for validation trials. Tantalum beads (1.6mm diameter) were implanted in four corners of each foam block and secured with superglue. The foam thus rigidly joins the beads and the bones, but also separates the beads from the surface of the bone to reduce artifacts which occur when implanted beads in or on cortical bone are CT scanned. Two beads were also implanted into the wand. Validation trials were performed for each of the six bones under two conditions: translation and rotation of the imbedded-bone foam blocks.

Each block was individually affixed to a linear stage via the wand to a 1-micron precision stepper-motor (ROB-09238, SparkFun Electronics, Niwok CO) with attached micrometer (Figure 3, bottom). Starting at the original position, each block was imaged and then translated 0, 0.1, 0.2, 0.3, 0.4, 0.5, 1, 2, 3, 4, 5, 10 and 15mm from the original position. At each position, the block was imaged at 1000 Hz for 0.1 seconds to yield 100 static stereo image pairs.

The block wand was then mounted to a precision gearbox coupled to a rotational potentiometer (6209 series, Measurement Specialties Inc., Hampton VA). Again starting from an original position, each block was imaged and then rotated to 0, 0.01, 0.02, 0.03, 0.04, 0.05, 0.1, 0.2, 0.3, 0.4, 0.5, 1, 2, 3, 4, 5 and 15 degrees from the original position. A 100 static frames captured at 1000 Hz were recorded in the same manner as the translational trials.

The imbedded-bone foam blocks were collectively CT scanned using a GE Discovery CT750 HD. The CT volume was reconstructed to form an isometric volume with voxel spacing of 0.4922 mm/voxel.

Pre-Processing

For each bone, 100 frames of fluoroscopic images were captured at each position. To reduce the number of frames to analyze, these data were decimated to yield 10 image frames for each translational or rotational position. Each bone was posed in 30 unique positions (translation and rotation together) which yield 300 frames per bone for a total of 1800 image pairs (Figure 4) to analyze in this study.

The session setup images of the distortion correction plate are used with a previously-reported algorithm [31] to generate a template. This template is applied to each frame of data to remove the in-plane distortion that arises during the fluoroscope acquisition (most notably the pincushion effect and magnetic lens distortion). The localizer / calibration block images are used to establish the relative 3D positions of the X-ray sources and the image acquisition planes [31]. This is done for each fluoroscope by first identifying each of the bead centroids in the fluoroscope image, and then calculating the direct linear transformation (DLT) matrix that relates the 2D positions of these beads to the corresponding 3D locations. This DLT calculation provides extrinsic and intrinsic camera parameters, which are necessary to generate our virtual imaging environment [32].

The CT scan of the imbedded-bone foam blocks was imported into custom segmentation software (Multi-Rigid [33]). This software provides a semi-automated method for segmenting bones. MultiRigid outputs two 3D volume datasets: scan intensity (bone density) information, and a label file that identifies which bone is contained by each voxel.

Bone Position Optimization

The major steps to determine bone position are: creation of digitally reconstructed radiographs (DRRs), manual setting of the initial bone pose, and algorithmic optimization of bone position.

A virtual imaging environment was formed in a coordinate system defined by the localizer / calibration block pre-processing. To create the DRRs, the 3D bone density and geometry data obtained from processing the CT scans in Multi-Rigid are imported into that virtual environment. In the virtual environment, X-rays are assumed to emit from a point source (the location of the focal spot) and project onto a virtual image intensifier focal plane. Thus a ray can be defined as extending from the virtual source, potentially though a virtual bone (depending on where the bone is positioned), to a given pixel on the virtual image intensifier. There are 1.03×10^6 pixels (and therefore rays) for each of the two virtual fluoroscope / intensifier pairs. The DRR is thus a 2D array of pixel intensity values with each intensity value corresponding to a numerical estimate of the integral of the CT voxel values along each of these rays.

A user of the biplane system interfaces with the optimization software through a graphical user interface (GUI). This GUI allows the user to view any frame in a data set, and select which bone to activate in the virtual imaging environment. Activated bones will display their 3D surface files, allowing the user to rapidly match bone pose with the fluoroscope image. To accomplish this, the user has a variety of positioning tools available to manually align the 3D bone surface in both fluoroscope views with the imaged bone. These include tools that allow the user to adjust the 3D bone position in individual 2D fluoroscope views, manually input rotation and translation values, and perform 3D rotation of the bone (Figure 5).

Once the user has performed a manual initial positioning of the bone, an automated optimization algorithm using a derivative-free optimizer (CONDOR) [34] is initialized. At each perturbation, the following steps occur:

- A DRR is generated for the bone pose.
- The horizontal and vertical gradients of each DRR are calculated.
- A binary mask is generated for the non-zero pixels of the DRR (i.e., the region where the bone projects onto the virtual image intensifier plane). This mask is dilated by several pixels.
- The horizontal and vertical gradients of the fluoroscope image are calculated.
- The binary mask is applied to the fluoroscope image and its gradients for subsequent analysis.
- NCCs (normalized correlation coefficients) are calculated for the pair of gradient images and for the pairs of intensity images.
- A final weighted sum of NCC values is calculated.

The optimizer iteratively perturbs the six degrees of freedom of each bone (three Euler angles and three centroid offsets) characteristic of rigid-body transformations. This is done until the overall NCC value was maximized; this position is deemed the "optimal" position for that bone / frame (Figure 5, area B). Typically, 200-250 DRRs must be generated for each pair of fluoroscope images before the optimized position is found.

For bone position optimization, both image intensities and image gradients (horizontal and vertical) from each of the two perspectives are used to evaluate the match between DRR and fluoroscope images. Intensity matching provides a coarse registration, while image gradients, which tend to accentuate object edges and similar features, provide fine adjustments to the registration (Figure 6).

Image gradients in the horizontal (G_H) and vertical (G_V) directions were calculated by means of image convolution. These gradient images were designed to make object edges more pronounced, which can aid in fine adjustments to the optimal bone position. The convolution kernel was a 2D Gaussian gradient kernel, which combined both differentiation and Gaussian blurring into a single convolution. The kernel K that was used to calculate the gradient in the x-direction (horizontal) direction was defined as:

$$K(u,v) = \frac{-u}{\sigma^4(2\pi)} e^{-\left(\frac{u^2+v^2}{2\sigma^2}\right)} \quad \text{[Equation 1]}$$

And thus the horizontal gradient image at pixel (x,y) was:

$$G_H(x,y) = \sum_{u=-N}^{N} \sum_{v=-N}^{N} K(x+u, y+v) * I(x,y) \quad \text{[Equation 2]}$$

For the present study, σ = 1.5 pixels and *N* = 6. To calculate the gradient in the vertical direction, *u* and *v* are swapped in Equation 1.

CONDOR's merit function relies on a user-specified weighted linear combination of intensity- and gradient-based NCC calculations. For each of the two fluoroscopes, three NCCs were calculated: (a) DRR intensity vs. masked fluoroscope intensity, (b) DRR horizontal gradient vs. masked fluoroscope horizontal gradient, and (c) DRR vertical gradient vs. masked fluoroscope vertical gradient.

These three NCCs are each weighted by a factor of (1/3) and summed; accordingly, the gradient NCCs are weighted twice as much (2/3) as the intensity NCCs, to promote fine adjustments of the registration. The weighted NCCs from the two fluoroscopes are then averaged together.

The NCC of two images *d* and *f,* both containing *n* pixels, is defined as:

$$NCC = \frac{\sum_{i=1}^{n}(d_i-\bar{d})(f_i-\bar{f})}{\sqrt{\sum_{i=1}^{n}(d_i-\bar{d})^2}\sqrt{\sum_{i=1}^{n}(f_i-\bar{f})^2}} \quad \text{[Equation 3]}$$

Where $\bar{d}$ and $\bar{f}$ are the mean values of images *d* and *f.* Thus, the NCC is the ratio of the dot product of the two images divided by the product of their standard deviations. These result in a total of five summations for each NCC: two summations to calculate the means, two sums of squared deviations, and one dot product (product of deviations).

Bead Position Optimization

Four tantalum beads were rigidly imbedded in corners of the foam blocks containing each bone (Figure 4). For each frame, the location of these beads in the frames was first determined using a template-matching algorithm [35]. Briefly, an 11x11 pixel template image of a bead was first defined from one frame. For each pixel in the full fluoroscope image, this template image was centered over the target pixel, and the NCC was calculated between the template image and the portion of the full image underlying the template image. The pixel locations in the full image where the NCC exceeded a specified threshold defined the bead locations for that frame. This was repeated for all frames in both fluoroscopes. The 2D bead locations were then converted to 3D coordinates using the DLT.

Post-Processing and Analysis

For the translational trials, the resulting global translation between each bone's or set of bead's frame-by-frame optimal transformation matrix was extracted for comparison to the precision linear stage. For the rotational trials, a screw axis was calculated for each frame for a given bone or set of beads. The rotation about this screw axis was extracted for comparison to the

precision rotational stage. The translation or rotation of the beads (relative to their initial locations) was then calculated and compared to their respective model-based calculations.

The bias of our optimization technique was defined as the root-mean-square (RMS) error of the difference between the known and calculated bone or bead position, each relative to the precision stage, while the precision was defined as the standard deviation of that difference [31].

Results

The overall bone-based translational bias of the six bones was 0.058 mm with a precision of ± 0.049. The overall bone-based rotational bias of the six bones was 0.291° with a precision of ± 0.268°. Considering individual bones in translation, all bones were tracked with comparable bias with the exception of one calcaneus (Calcaneus B) (Figure 7, left). The talus from the same specimen optimized consistently like the other bones. Considering individual bones in rotation, the results of the performance of the six bones are given (Figure 7, right).

The magnitude of rotational and translational errors for bead tracking was similar to the bone results. The overall translational bias of the bead tracking was 0.037 mm with a precision of ± 0.032 mm. The overall rotational bias of the bead tracking was 0.292° with a precision of ± 0.263°.

Our central processing unit (CPU) bone-based optimization algorithm averages 300 ms per DRR generation. The optimization of a single bone in a single frame took on average 6-8 minutes. While some automated optimization trials drifted into a grossly wrong position, this was rare and most optimizations completed without requiring a restart of the optimization.

Discussion

Algorithm Performance: The primary goal of this paper was to demonstrate the function and capability of our custom created model-based tracking software. We have presented a method for optimizing bone pose and validated that method by tracking several bones of interest in the foot and ankle. The bias and precision of our model-based tracking method (0.058 ± 0.049 mm for translation and 0.291 ± 0.268° for rotation) was determined by comparison to the precision linear / rotational stage. By collecting precision stage, bead- and model-based data, we also have the ability to evaluate how bead-based results compare against a higher resolution standard (the precision stage). A secondary goal was to determine the bias and precision of our bead-based tracking method (0.037 ± 0.032mm for translation and 0.292 ± 0.263° for rotation), which was found to be comparable. Thus we achieved both goals, as the model- and bead-based tracking both demonstrated sub-millimeter and sub-degree bias and precision, indicating

our ability to track several isolated bones of the foot and ankle (the talus, calcaneus and first metatarsal) during 1000 Hz fluoroscopic imaging.

The performance of our system compares well to prior validations using the biplane fluoroscopy technique. At the hip: Martin et al. found model-based bias averages (for single bones) that did not exceed 0.21 mm, with precision values that reached a maximum of 0.22 mm for the femur and 0.24 mm for the pelvis [18]; Lin et al. determined static (bias ± precision) values of 0.60 ± 0.75 mm and 0.69 ± 0.85° when imaging the pelvis and femur, respectively. At the knee: Anderst et al. found that the only significant bias in their system related to the z-axis position of the tibia (−0.37 ± 0.13mm). They also reported an overall model-based precision for static trials which ranged from 0.030 to 0.080 mm (noted as depending on laboratory axis direction, with less precision for x-axis) [21]; Bey et al. considered differences between bead- and model-based techniques, finding a bias which ranged from -0.174 to 0.248 mm (reported to depend on coordinate direction) and a precision which ranged from 0.023 to 0.062 mm [25]. At the ankle, and most germane to this study, Caputo et al. implanted markers in the tibia, talus and calcaneus then performed five tracking trials in each of three positions of the ankle (neutral, dorsiflexion, and plantar flexion). Comparing the marker to the model-based results, they determined an average error in tibiotalar kinematics of 0.04 ± 0.11mm (in joint displacement) and 0.2 ± 0.1° (in joint rotation) [23]. In summary: numerous biplane systems, employed to study joints at all levels in the lower extremity, have been consistently validated to demonstrate their ability to track motion in sub-millimeter and sub-degree ranges, as our system has now been shown to.

The bead tracking results of this work are significant in that they demonstrate errors of similar magnitude to the model-based results; both validations are performed against a standard with a resolution at least an order of magnitude better. This issue has been previously discussed in the literature: Anderst et al. noted the limitations of bead-based tracking due to this resolution concern, but also stated the necessity to validate during an *in vivo* dynamic motion, which requires the use of beads as the gold standard [21]. Bey et al. also acknowledge the usefulness of measuring to an order of magnitude better than the smallest change of interest [25]. It should be noted that clinically relevant effect sizes may vary between different joints; Brainerd et al. described the difficulty of validating the motion of small bones with beads [36], a concern which is particularly important in the study of the foot and ankle joints; Miranda et al. also noted similar magnitudes of error in their marker-based and markerless tracking when compared to a precision stage-based gold standard [37]. By validating our data to a precision stage, and by positioning beads within blocks larger than the bones, we generated very rigorous reference data to compare to the model-based tracking performance.

Both methods (beads vs. precision stage) have advantages and disadvantages. The advantage of using beads as the gold standard is that complex and dynamic motions can readily be tested and validated using actual joints, whether *in vivo* or *in vitro*. The disadvantage is that the error magnitude of beads as a gold standard is similar to that of model-based tracking. The advantage of using a precision stage as the gold standard is the improvement in its measurement resolution, but this comes with the technical limitation of being unable to simulate natural movement during validation.

There are some limitations to this work. First we did not image bones in their native environment (the foot), but instead imaged them in isolation from neighboring bones and from their enveloping soft tissue. We also imaged static positions of the bones and not dynamic movement. Additionally, our processing time requires several hours for a single bone to be tracked during less than a second of fluoroscope image capture (i.e., a gait cycle). While this processing time is being addressed through system improvements (e.g., graphical processing unit (GPU)-based programming), the time currently required limits the use of this system to research studies. We did not simulate a physiological motion as our precision stages were limited to uni-axial translation and rotation of the bones. We mitigated these effects by translating bones along a direction which is similar to subject's path of travel through the imaging field in vivo, and our rotational axis was chosen for each bone to approximately correspond to the primary axis of internal and external rotation of the foot. We also analyzed single frames captured at 1000Hz, a frequency which would eliminate motion blur artifact during dynamic imaging, rendering our static frame quality similar to the quality expected during dynamic imaging. Regarding our bead-based tracking, by imbedding the beads in a foam block we increased our inter-bead distances, which could artificially improve the accuracy of our bead-based measurement. This was done so that the foam block protected the bone from bead imaging artifact (by increasing bead-bone surface distance) during the CT scan. A final concern is related to the anatomical shape of the bones affecting the bias. For example, in rotation the results of the tali appear less accurate than the calcanei or first metatarsals (Figure 7, right), though it should be noted that these observations are only anecdotal at this point (n=2 for each bone). However, it is reasonable to surmise that bones which exhibit some amount of axial symmetry, and bones which are very small, may both track less well than large and uniquely shaped bones – both of these issues may be of greater concern when studying the foot vs. other joints of the lower extremity.

Conclusions

The validation of our model-based tracking algorithm is a vital step towards using this technology in research and clinical settings. The benefits (a better standard) and drawbacks (limited motion) of using precision stage data for validation, as opposed to bead-tracking, has

been investigated. In the future, we plan to explore improved methods to achieve faster optimization times, and improvements to the tracking algorithm to accurately track the entire pantheon of bones within the intact foot.

In summary, due to the high level of dependence this technology has on the anatomy / joint of interest it is used to measure, we have demonstrated accurate and precise tracking of a set of bones which are of interest in foot and ankle kinematics. Talar and calcaneal kinematics are necessary to parse the kinematics of the hindfoot faithfully into ankle and subtalar joint motions. We have demonstrated our ability to track these bones. Further, the first metatarsal plays a key role in many forefoot pathologies, as well as having significant use in the determination of overall foot shape and deformity. By testing our methodology against these key structures, we have validated our use of biplane fluoroscopy to study pathologies and treatments of the foot and ankle.

Figure Captions

Figure 1: (Left) Aluminum distortion correction plate with 3 mm holes in a 1.5 cm precision pattern. Note the unique pattern of the larger (5 mm) holes which is used for automatic orientation of the image. (Center) Fluoroscopic image of the distortion correction plate prior to the application of the corrective mapping – lower right enlargement shows known hole pattern, a.k.a. control points (black dots) with displacement error (white lines) mapping them to the imaged hole pattern (grey circles). (Right) Fluoroscope image of the distortion correction plate after the application of the corrective mapping – lower right enlargement shows control points aligned with holes in the corrected image.

Figure 2: (Left) Image localizer / calibration block, note the various bead sizes and unique 3D pattern. (Right) Fluoroscope image of the localizer block showing bead size and pattern.

Figure 3: (Top) Bones imbedded in foam block on CT scan bed; the amount of foam surrounding blocks was chosen to give a buffer between the bone and the tantalum beads imbedded in the wand (black stalk) and foam corners – tantalum beads can cause surface artifact if near bone in CT scans. (Bottom) Imaging experimental setup: (A) X-ray emitters, (B) linear / rotational stage setup, here configured for rotation, and (C) foam block with calcaneus imbedded.

Figure 4: (Left) Fluoroscopy image of calcaneus A from the "blue" and (Right) "green" systems. Note the location of the wand connection to the precision stage (white line, left image). Also visible are tantalum beads which are glued into the extreme edges of the foam block, with two additional beads in the wand. The foam block is barely visible due to its low density; the plastic collar connecting the wand to the foam block is visible (white line, right image).

Figure 5: Graphical user interface (GUI) for the initial position / optimization software. Shown is the same frame of calcaneus A from Figure 4. We label the two fluoroscopes as "blue" and "green" (left and right sets of fluoroscope views in this figure). Each image contains the fluoroscope image, and a 3D bone surface overlays (and surface centroids as large dots). The top pair of images (A) represents an un-optimized DRR (light bone shadow) / fluoroscope (dark bone shadow) configuration showing poor overlap, the bottom pair of images (B) represent an optimized DRR / fluoroscope configuration showing complete overlap.

The bottom portion of this figure shows the control and indicator windows for the GUI. The bone surfaces in this image update in real time as the position of the initial guess is manually adjusted. The user can adjust the initial position of bones by any combination of: mouse drag of the 3D bone overlay within the 2D fluoroscope image panes, entering numerical values into the "current pose" table, and performing a 3D manipulation of the bone (lower right graphic). NCC values are displayed as separate breakdowns of intensity vs. gradient for each view ("blue" and

"green"), as well as final weighted NCC. Frame advance, key frame, and saving features are built in to aid the user.

Figure 6: (Left) Vertical gradient and (Right) horizontal gradient of the DRR of calcaneus A for the "blue" fluoroscope (the "green" fluoroscope was handled similarly). These images are separately compared using the NCC to the fluoroscope image gradients.

Figure 7: Performance of the algorithm to track each of the six bones during complete translation trials, along with the average overall translational bias and precision for the six cadaveric bones tested (left). And similar summary for the rotational performance of the six bones is also includes (right). Met = First Metatarsal, Calc = Calcaneus.

Figure 8: Performance of the algorithm to track the bead sets for each of the six bones during translation trials, along with the average overall translational bias and precision for the six bead sets tested (left). And similar summary for the rotational performance of the six bead sets is also included (right). Met = First Metatarsal, Calc = Calcaneus.

Acknowledgements

This work was supported in part by Merit Review Awards F7468R and A1070R from the United States (U.S.) Department of Veterans Affairs Rehabilitation Research and Development Service. The authors also wish to thank Eric Thorhauer for critiquing the manuscript.

Competing interests: None declared

Ethical approval: Not required

References

[1] De Mits S, Segers V, Woodburn J, Elewaut D, De Clercq D, Roosen P. A clinically applicable six-segmented foot model. J Orthop Res. 2012;30,655-661.

[2] Kidder SM, Abuzzahab FS, Jr., Harris GF, Johnson JE. A system for the analysis of foot and ankle kinematics during gait. IEEE Trans Rehabil Eng. 1996;4:25-32.

[3] Carson MC, Harrington ME, Thompson N, O'Connor JJ, Theologis TN. Kinematic analysis of a multi-segment foot model for research and clinical applications: a repeatability analysis. J Biomech. 2001;34:1299-307.

[4] Jenkyn TR, Nicol AC. A multi-segment kinematic model of the foot with a novel definition of forefoot motion for use in clinical gait analysis during walking. J Biomech. 2007;40:3271-8.

[5] Caravaggi P, Benedetti MG, Berti L, Leardini A. Repeatability of a multi-segment foot protocol in adult subjects. Gait Posture. 2011;33:133-5.

[6] Jenkyn TR, Anas K, Nichol A. Foot segment kinematics during normal walking using a multisegment model of the foot and ankle complex. J Biomech Eng. 2009;131:034504.

[7] MacWilliams BA, Cowley M, Nicholson DE. Foot kinematics and kinetics during adolescent gait. Gait Posture. 2003;17:214-24.

[8] Khazzam M, Long JT, Marks RM, Harris GF. Preoperative gait characterization of patients with ankle arthrosis. Gait Posture. 2006;24:85-93.

[9] Chimenti RL, Tome J, Hillin CD, Flemister AS, Houck J. Adult-acquired flatfoot deformity and age-related differences in foot and ankle kinematics during the single-limb heel-rise test. J Orthop Sports Phys Ther. 2014;44:283-90.

[10] Cappello A, Stagni R, Fantozzi S, Leardini A. Soft tissue artifact compensation in knee kinematics by double anatomical landmark calibration: performance of a novel method during selected motor tasks. IEEE Trans Biomed Eng. 2005;52:992-8.

[11] Tranberg R, Karlsson D. The relative skin movement of the foot: a 2-D roentgen photogrammetry study. Clin Biomech (Bristol, Avon). 1998;13:71-6.

[12] Shultz R, Kedgley AE, Jenkyn TR. Quantifying skin motion artifact error of the hindfoot and forefoot marker clusters with the optical tracking of a multi-segment foot model using single-plane fluoroscopy. Gait Posture. 2011;34:44-8.

[13] Gao B, Zheng NN. Investigation of soft tissue movement during level walking: translations and rotations of skin markers. J Biomech. 2008;41:3189-95.

[14] Peters A, Galna B, Sangeux M, Morris M, Baker R. Quantification of soft tissue artifact in lower limb human motion analysis: a systematic review. Gait Posture. 2010;31:1-8.

[15] Nester C, Jones RK, Liu A, Howard D, Lundberg A, Arndt A, et al. Foot kinematics during walking measured using bone and surface mounted markers. J Biomech. 2007;40:3412-23.

[16] Li K, Zheng L, Tashman S, Zhang X. The inaccuracy of surface-measured model-derived tibiofemoral kinematics. J Biomech. 2012;45:2719-23.

[17] Li G, DeFrate LE, Park SE, Gill TJ, Rubash HE. In vivo articular cartilage contact kinematics of the knee: an investigation using dual-orthogonal fluoroscopy and magnetic resonance image-based computer models. Am J Sports Med. 2005;33:102-7.

[18] Martin DE, Greco NJ, Klatt BA, Wright VJ, Anderst WJ, Tashman S. Model-based tracking of the hip: implications for novel analyses of hip pathology. J Arthroplasty. 2011;26:88-97.

[19] Lin H, Wang S, Tsai TY, Li G, Kwon YM. In-vitro validation of a non-invasive dual fluoroscopic imaging technique for measurement of the hip kinematics. Med Eng Phys. 2013;35:411-6.

[20] Li G, Defrate LE, Rubash HE, Gill TJ. In vivo kinematics of the ACL during weight-bearing knee flexion. J Orthop Res. 2005;23:340-4.

[21] Anderst W, Zauel R, Bishop J, Demps E, Tashman S. Validation of three-dimensional model-based tibio-femoral tracking during running. Med Eng Phys. 2009;31:10-6.
[22] de Asla RJ, Wan L, Rubash HE, Li G. Six DOF in vivo kinematics of the ankle joint complex: Application of a combined dual-orthogonal fluoroscopic and magnetic resonance imaging technique. J Orthop Res. 2006;24:1019-27.
[23] Caputo AM, Lee JY, Spritzer CE, Easley ME, DeOrio JK, Nunley JA, 2nd, et al. In vivo kinematics of the tibiotalar joint after lateral ankle instability. Am J Sports Med. 2009;37:2241-8.
[24] Wang B, Roach KE, Kapron AL, Fiorentino NM, Saltzman CL, Singer M, et al. Accuracy and feasibility of high-speed dual fluoroscopy and model-based tracking to measure in vivo ankle arthrokinematics. Gait Posture. 2015;41:888-93.
[25] Bey MJ, Kline SK, Tashman S, Zauel R. Accuracy of biplane x-ray imaging combined with model-based tracking for measuring in-vivo patellofemoral joint motion. J Orthop Surg Res. 2008;3:38.
[26] Bey MJ, Zauel R, Brock SK, Tashman S. Validation of a new model-based tracking technique for measuring three-dimensional, in vivo glenohumeral joint kinematics. J Biomech Eng. 2006;128:604-9.
[27] Anderst WJ, Baillargeon E, Donaldson WF, 3rd, Lee JY, Kang JD. Validation of a noninvasive technique to precisely measure in vivo three-dimensional cervical spine movement. Spine (Phila Pa 1976). 2011;36:E393-400.
[28] Massimini DF, Warner JJ, Li G. Non-invasive determination of coupled motion of the scapula and humerus--an in-vitro validation. J Biomech. 2011;44:408-12.
[29] McDonald CP, Bachison CC, Chang V, Bartol SW, Bey MJ. Three-dimensional dynamic in vivo motion of the cervical spine: assessment of measurement accuracy and preliminary findings. Spine J. 2010;10:497-504.
[30] McDonald CP, Moutzouros V, Bey MJ. Measuring dynamic in-vivo elbow kinematics: description of technique and estimation of accuracy. J Biomech Eng. 2012;134:124502.
[31] Iaquinto J, Tsai R, Haynor D, Fassbind M, Sangeorzan BJ, Ledoux WR. Marker-Based Validation of a System for the Dynamic Investigation of 3D Joint Kinematics using Biplane Fluoroscopy. Medical Engineering & Physics. 2012.
[32] Melen T. Geometrical modelling and calibration of video cameras for underwater navigation [Ph.D. Thesis]: Institute for Teknisk Kybernetikk; 1994.
[33] Hu Y, Ledoux WR, Fassbind M, Rohr ES, Sangeorzan BJ, Haynor D. Multi-rigid image segmentation and registration for the analysis of joint motion from three-dimensional magnetic resonance imaging. J Biomech Eng. 2011;133:101005.
[34] Berghen V. Optimization Algorithm for Non-Linear, Constrained, Derivative-free Optimization of Continuous, High-computing-load Functions. [IRIDIA Technical Report]. Belgium: Universite Libre de Bruxelles; 2004.
[35] Lewis J. Fast normalized cross-correlation. Vision Interface. 1995;10:120-3.
[36] Brainerd EL, Baier DB, Gatesy SM, Hedrick TL, Metzger KA, Gilbert SL, et al. X-ray reconstruction of moving morphology (XROMM): precision, accuracy and applications in comparative biomechanics research. J Exp Zool A Ecol Genet Physiol. 2010;313:262-79.
[37] Miranda DL, Schwartz JB, Loomis AC, Brainerd EL, Fleming BC, Crisco JJ. Static and dynamic error of a biplanar videoradiography system using marker-based and markerless tracking techniques. J Biomech Eng. 2011;133:121002.

Figure

Click here to download high resolution image

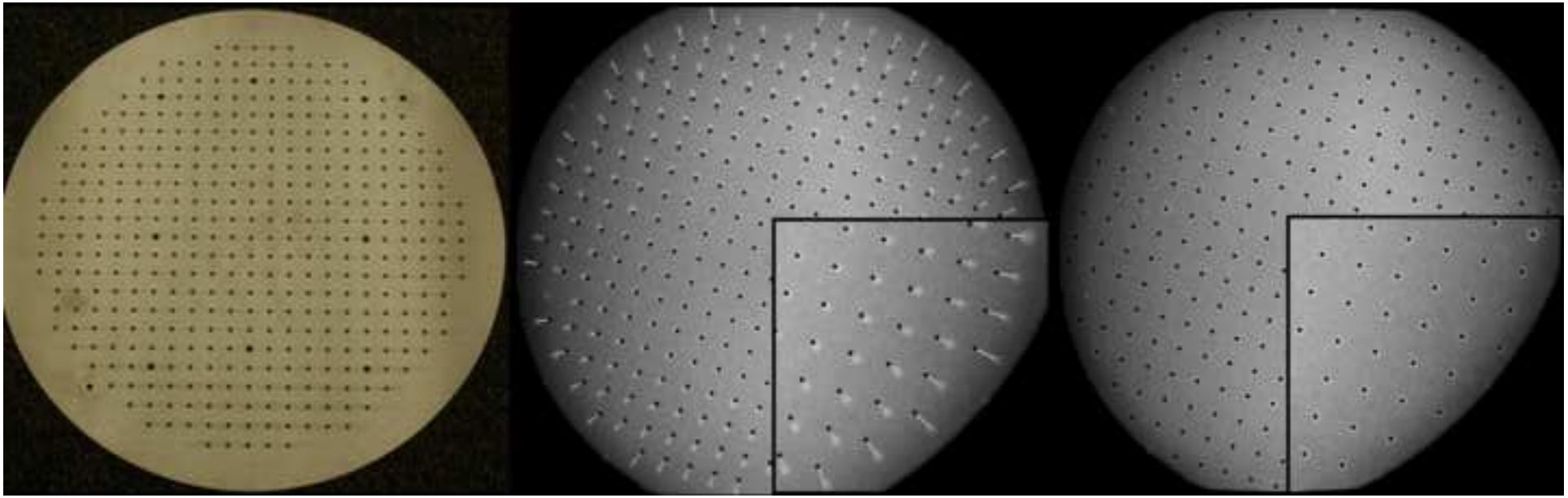

Figure

Click here to download high resolution image

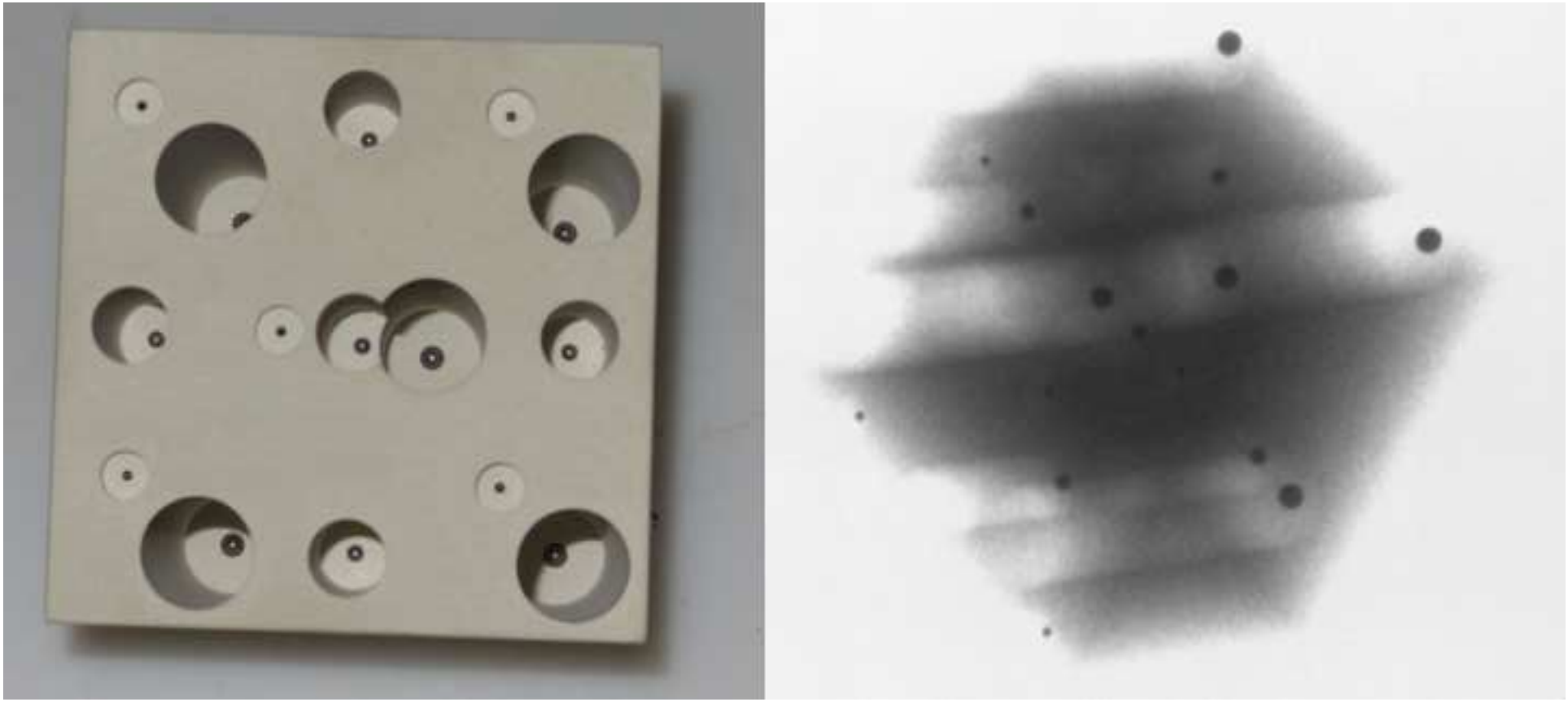

Figure

Click here to download high resolution image

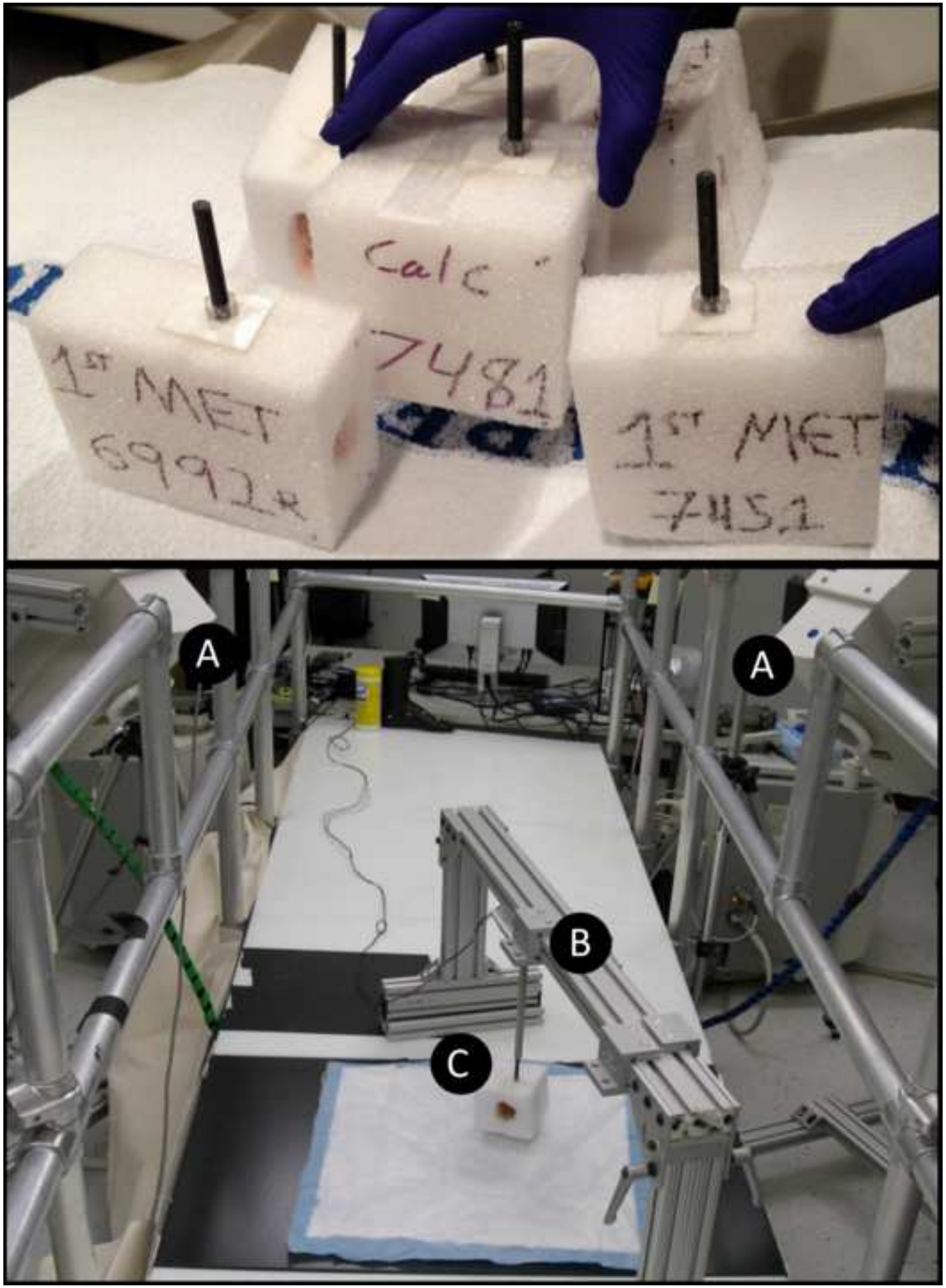

Figure

Click here to download high resolution image

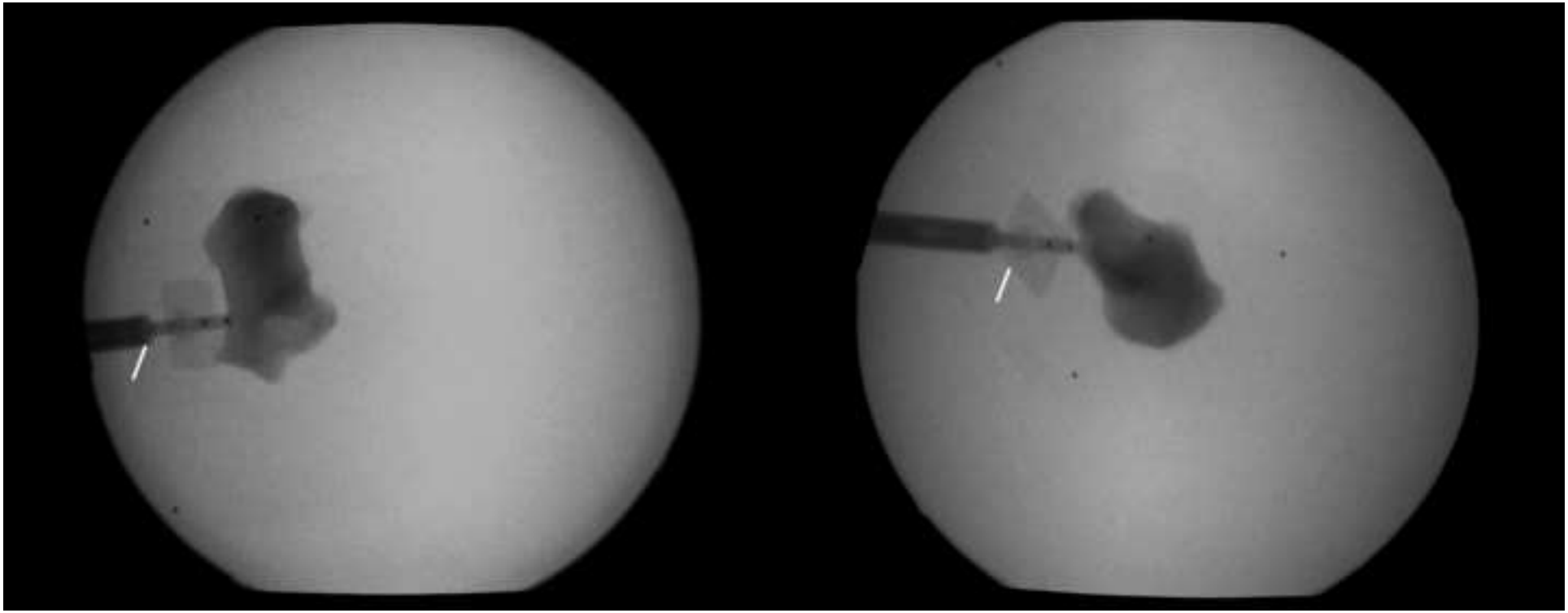

Figure

Click here to download high resolution image

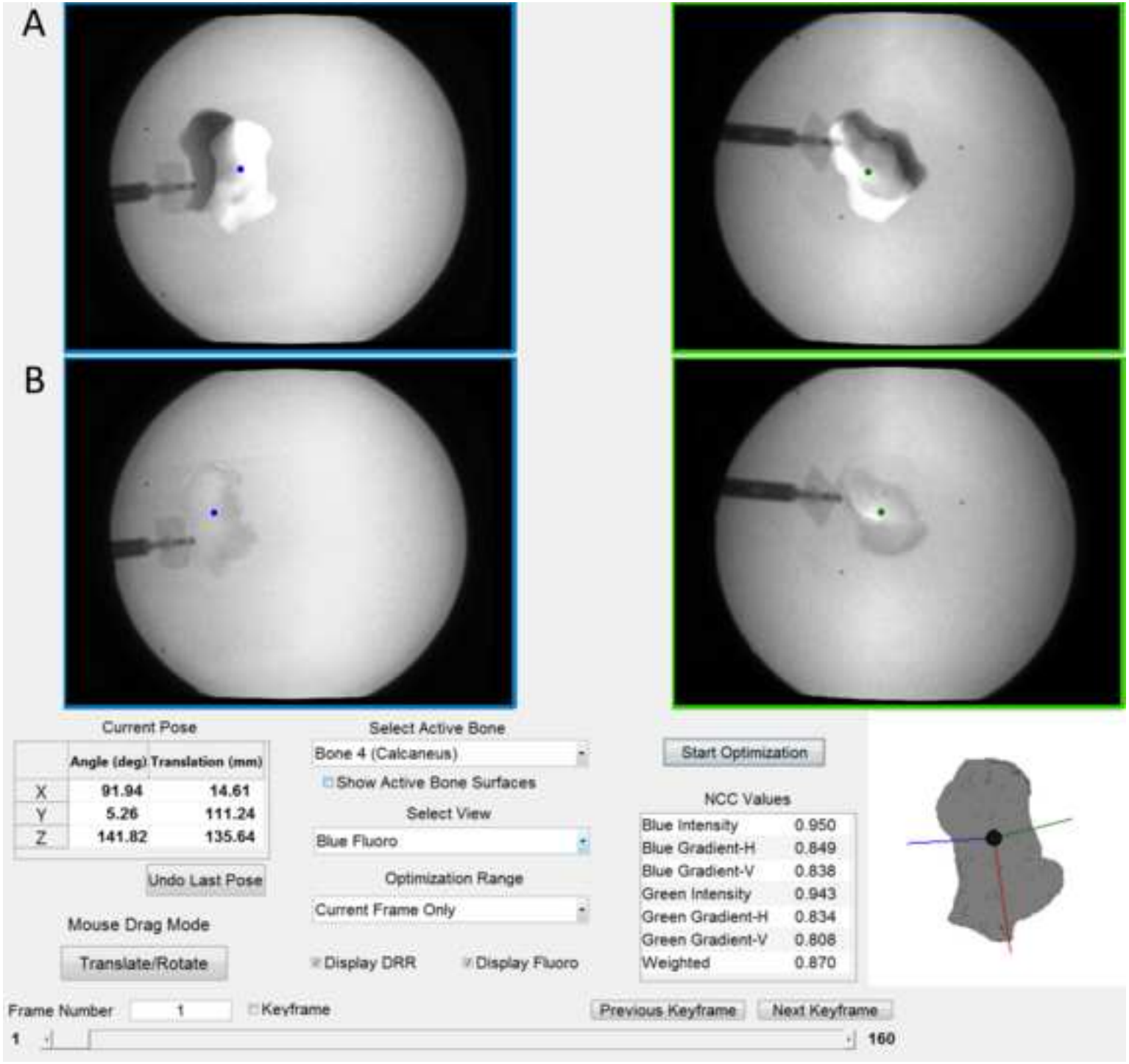

Figure

Click here to download high resolution image

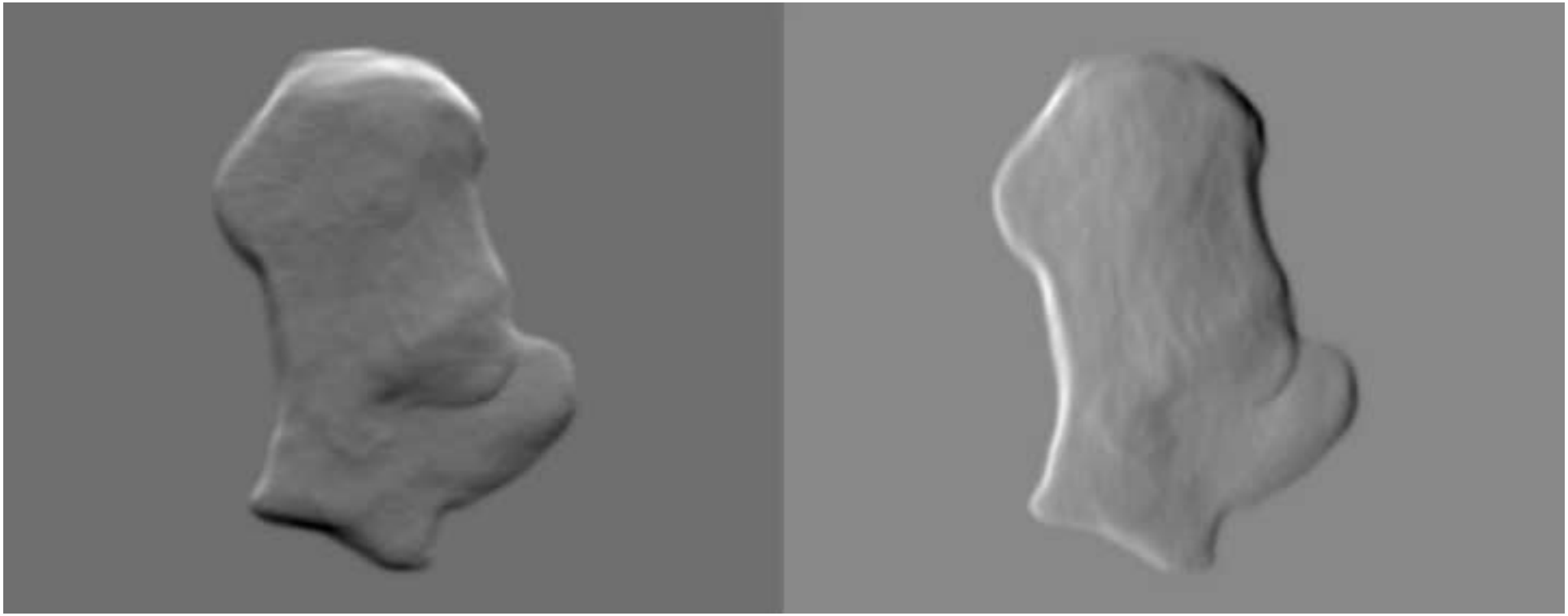

Figure

Click here to download high resolution image

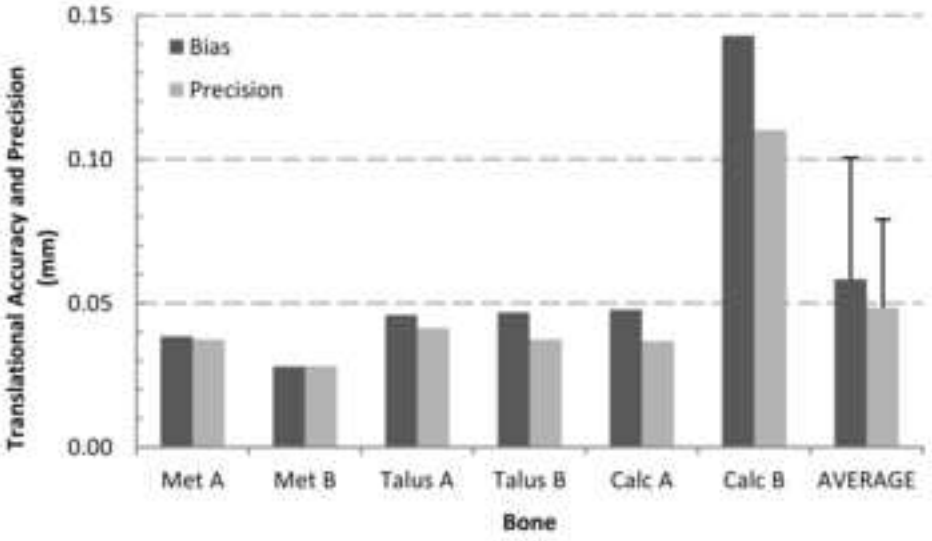

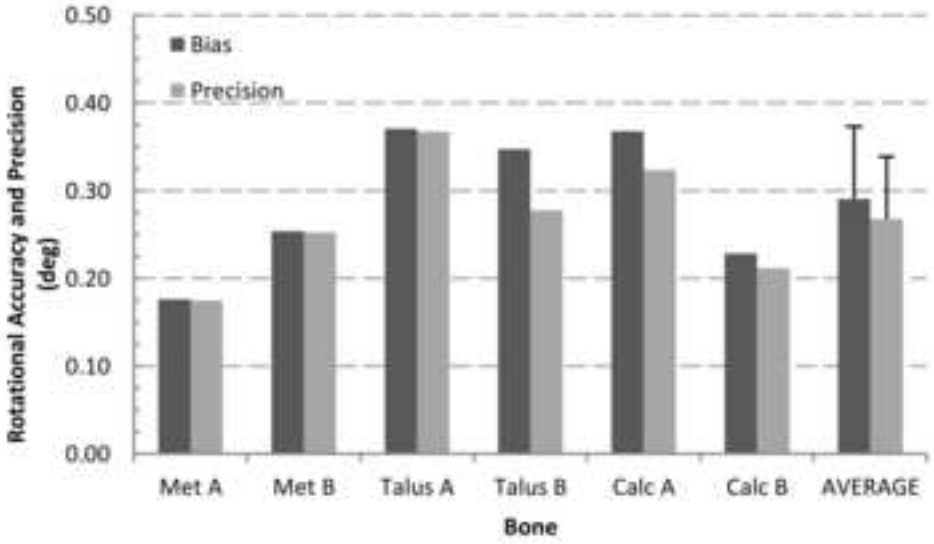

Figure

Click here to download high resolution image